Analysis of toroidal phasing of resonant magnetic perturbation effects on edge transport in the DIII-D tokamak

T. M. Wilks, W. M. Stacey, and T. E. Evans

Additional information on Phys. Plasmas

Analysis of toroidal phasing of resonant magnetic perturbation effects on edge transport in the DIII-D tokamak

T. M. Wilks,[1,a)] W. M. Stacey,[1] and T. E. Evans[2]
[1]*Georgia Institute of Technology, Atlanta, Georgia 30332, USA*
[2]*General Atomics, San Diego, California 92186, USA*

Resonant Magnetic Perturbation (RMP) fields produced by external control coils are considered a viable option for the suppression of Edge Localized Modes in present and future tokamaks. In DIII-D, the RMPs are generated by six pairs of I-coils, each spanning 60° in toroidal angle, with the currents flowing in opposite directions in adjacent pairs of I-coils. Reversal of the currents in all I-coils, which produces a 60° toroidal shift in the RMP field configuration, generates uniquely different edge pedestal profiles of the density, temperature, and rotation velocities, implying different effects on the related edge transport phenomena caused by the difference in toroidal phase of the I-coil currents. The diffusive and non-diffusive transport effects of this RMP toroidal phase reversal are analyzed by comparing the ion and electron heat diffusivities, angular momentum transport frequencies, ion diffusion coefficients, and the particle pinch velocities interpreted from the measured profiles for the two phases of the I-coil currents. © *2013 AIP Publishing LLC*.
[http://dx.doi.org/10.1063/1.4804350]

I. INTRODUCTION

In 1980s, a regime of enhanced plasma confinement, H-mode, was discovered in the ASDEX tokamak in Germany.[1] H-modes can achieve high plasma pressure normalized by the confining magnetic field and features relatively flat profiles of temperature, pressure, and density across the core and sharp gradients in the plasma edge. These profiles are said to sit on a "pedestal" because of this structure.

However, the superior confinement in H-mode comes with a price. Magneto-hydrodynamic instabilities called "edge localized modes" (ELMs) are caused by the large edge pressure gradients and the resulting bootstrap currents in the edge pedestal region. ELMs are cyclical instabilities that spew plasma particles and energy from the edge region over a very short time interval.[2] The ELM degrades confinement and introduces large heat and particle fluxes to the first wall and the divertor plate, which can be detrimental to the integrity of plasma facing materials and discharge performance in fusion reactors such as ITER.[3]

Resonant magnetic perturbations (RMPs) have been identified as a means for both mitigating and suppressing ELMs, while maintaining a steady state H-mode plasma[4] with a decrease in performance in terms of H98 or plasma beta factor under some conditions. In DIII-D, external resonant magnetic perturbation fields are applied to the tokamak by currents in non-axisymmetric, three-dimensional, coils placed inside the vacuum region between the graphite first wall and the stainless steel vessel wall. RMPs induce radial transport,[5] decreasing the density gradient (and temperature gradient to a smaller degree[6]), which acts to lower the pressure gradient below the peeling-ballooning mode ELM threshold. RMPs can also be used to change the characteristics of the ELM, so that the

beneficial effect of impurity removal can be retained while the detrimental effect of increased heat flux on the divertor plate can be mitigated.

There has been widespread research on the effect of RMP fields on toroidal plasmas over the past decade. Edge pedestal profiles in "matched" RMP and H-mode shots[7] have been analyzed by comparing density and temperature profiles, confinement times, and particle fluxes on the divertor plate,[8] as well as the role of particle pinch in the generation of a transport barrier for both scenarios.[5] Active control methods have been investigated to manipulate the safety factor profile in order to determine the window of resonance operation when ELMs are suppressed.[9] The dependence of the effect of RMP on plasma shape[10] and collisionality[11] has been investigated with particular emphasis on ITER similar scenarios. In addition, the effect of RMP fields on magnetic islands and overlapping islands to generate an edge stochastic region has also been assessed.[12] There has been previous research on the effect of RMPs on magnetic braking via electromagnetic torque using resonant harmonics in the applied field as well as the neoclassical toroidal viscosity model by applying non-resonant harmonics.[12,13]

Prior analysis of RMP effects with respect to H-mode, safety factor, plasma shape, collisionality, toroidal rotation, and edge stochastic regions has laid the groundwork for designing the RMP coil layout for ITER. However, the theoretical framework for the differences in edge transport when the toroidal phase of the I-coil current producing the RMP in DIII-D changes is not fully understood. There are toroidal asymmetries in the "background" magnetic field in DIII-D, which is a likely cause for the different edge profiles and implied differences in edge transport observed when the toroidal phase of the RMP field is changed. The purpose of the present work is to examine this difference in edge transport between RMPs that have been applied with different toroidal

a)Electronic mail: theresa.wilks@gatech.edu

phases, i.e., by the different resonant magnetic fields generated by currents flowing through I-coils with different toroidal phases.

The RMPs considered in this paper are of toroidal mode number n = 3 that resonate in the edge region to enhance ion transport and decrease electron density and pressure,[9] but do not greatly affect the core of the plasma. Basic conservation laws of particle, momentum, and energy balances are employed to interpret both diffusive and non-diffusive transport from measured density, temperature, and rotation velocity profiles in the edge pedestal.[15] Interpretation of transport parameters, such as diffusion coefficients, pinch velocities, and momentum transfer frequencies, is used with the fluid conservation requirements[15] as a constraint for experimental data to characterize the dominant mechanisms for particle transport for each toroidal phase of the I-coil currents. The motivation for this work is to understand the fundamental transport changes caused by varying the I-coil phase in order that this effect can be exploited in future reactors to suppress ELMs in the most effective way.

II. RESONANT MAGNETIC PERTURBATIONS IN DIII-D SHOT 147170

Resonant magnetic perturbations are produced by magnet coils located in the vacuum region behind the plasma facing graphite tiles of the tokamak. These externally produced non-axisymmetric radial magnetic fields are manipulated to control edge pedestal plasma profiles, which result in the mitigation or suppression of ELMs. The RMP can be used to lower the magnitude and increase the frequency of ELMs to lessen in the impact on plasma facing components; or in some cases, completely stifle the ELMs altogether.[4]

The physical mechanisms concerning how the RMP changes these plasma parameters are only beginning to be understood. The RMPs tend to decrease the edge pedestal density,[5] which in turn decreases the pressure gradient to below the peeling-ballooning mode ELM instability threshold. One theory behind this concept is that the RMP produces a "density pump-out"[16] in the edge region, by causing radial particle streaming outward along the perturbed field lines as a mechanism for diminishing density, and therefore ELM suppression. Another possibility is that radial excursion of the magnetic field lines provides a "braking" of the plasma rotation, which affects the plasma force balance.[14] There are many ways to apply such a resonant perturbation, and the next step is to determine the most effective way to suppress ELMs while maintaining impurity control and energy confinement.

Different resonant magnetic perturbations are produced in DIII-D by changing the parity, magnitude, and toroidal phase of the externally applied magnetic fields. The two types of non-axisymmetric coils used are C-coils for field error correction and I-coils for RMP fields. As shown in Fig. 1, the C-coils are located parallel to the DIII-D tokamak axis outside of the vacuum vessel wall. Six I-coil pairs, each with one upper loop and one lower loop, are located toroidally symmetrically around the plasma behind the graphite tiles of the first wall that are facing the plasma. The RMP is said to
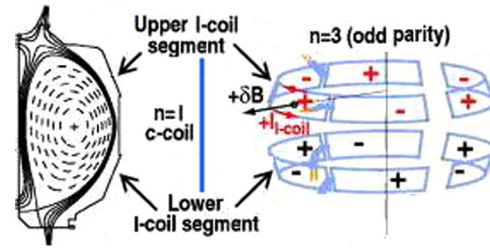

FIG. 1. Schematic of I-coil and C-coil magnet locations for DIII-D RMP shot 147170.[17] Reprinted with permission from R. A. Moyer *et al.*, Phys. Plasmas **12**, 056119 (2005). Copyright 2005 American Institute of Physics.

have even parity when the current in the upper and lower coils of each pair is flowing in the same direction and odd parity when the currents are opposite in the upper and lower coils of a coil pair. The toroidal phase of the I-coil field is defined in reference to the direction of current running through the upper coil located at the 30° (clockwise from North) measurement location on the tokamak.

DIII-D shot 147170 uses a toroidal mode number n = 3 in the I-coils for RMP ELM suppression and n = 1 in the C-coils for field error correction. A Toroidal mode number of three produces a resonance at n = 3 rational surfaces such as q = m/n = 11/3, where m is the poloidal mode number and q is the safety factor. For this shot, the I-coils have even parity and each adjacent set of I-coils produces a radial magnetic field in the opposite direction. Every 200 ms, the current in the I-coil reverses direction, and therefore the toroidal phase changes from 0° to 60° or vice versa. This process repeats and generates a toroidally shifting resonant magnetic perturbation field structure, along with a change in the edge pedestal transport. Currents running through the I-coil oscillate between roughly −4 kA to +4 kA to produce a non-axisymmetric radial perturbation field of about 15 Gauss, as shown in Fig. 2, based on modeling with the TRIP3D code,[18] which includes models describing the DIII-D field-errors.[19] The six constant C-coil currents used for the field-error correction are 975, −35, −1030, −975, 35, and 1030 A. There is a "background" radial
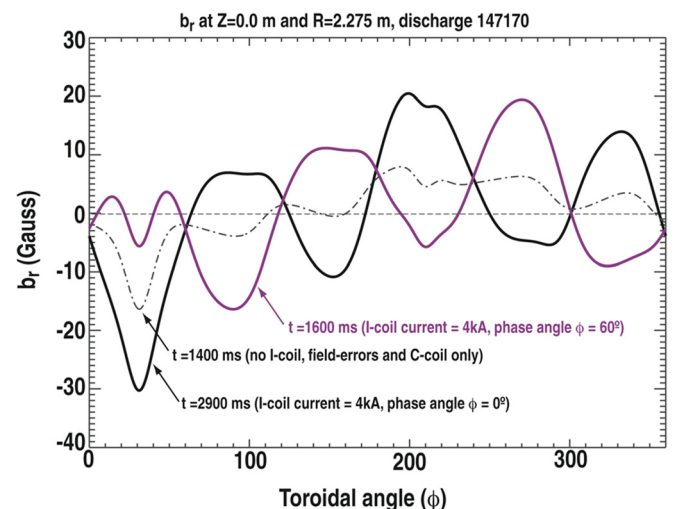

FIG. 2. Toroidal dependence of 0° and 60° radial magnetic fields produced by n = 3 I-coils superimposed with the "background" field. "Background" error field is produced by intrinsic field-errors and the n = 1 C-coil.[20]

field generated by equilibrium coils, including the C-coils but not the I-coils, shown as the 30° reference phase. Note that if the "background" radial field were axisymmetric, then reversing the toroidal phase between 0° and 60° would only shift the field perturbation around the torus by 60°, which would result in the same toroidal dependence of the radial perturbation due to the symmetric nature of a torus and the layout of the I-coils around the tokamak. A nulled "background" field would, therefore, have no effect on the plasma parameters because it would simply be redefining the reference position for the toroidal angle φ.

However, as indicated in Fig. 2, there is a -15 Gauss non-axisymmetric "background" radial field component, centered at $\varphi = 30°$, that constructively interferes with the 0° phase and destructively interferes with the 60° phase angle. This field results from the geometry of the buss bar connections used to power the toroidal magnetic field coils on DIII-D. It is superimposed on a toroidally varying set of field-errors due to small ($=<1$ cm) radial shifts in several poloidal field coils.[19] The C-coil is used in DIII-D discharge 147170 to correct these field-errors on the q = 2 surface in order to prevent locked modes. As seen in Fig. 2, the C-coil correction field produces an n = 1 residual field on the equatorial plane of the discharge at the separatrix location on the low-field side of the discharge. This is approximately 2 cm outside the top of the pedestal where the m/n = 11/3 resonant surface is located. This n = 1 residual field modulates the n = 3 field from the I-coil causing a toroidal variation that produces an asymmetry in the 0° and 60° phases as shown in Fig. 2.

Figure 2 suggests the toroidal dependence of the radial perturbed magnetic field as a possible cause of the difference between plasma parameters obtained for the 0° and the 60° RMP phases analyzed in this paper. Transport changes due to a local shift in the magnetic topology from the RMP are assumed to be negligible because vacuum field magnetic islands are screened to some extent in the outer pedestal region and are roughly an order of magnitude smaller than diagnostic resolution.[20] Further evidence supporting RMP impact on confinement arises in measured changes in global plasma parameters. Reversing the phase from 60° to 0° changes the plasma stored energy from 0.96 MJ to 1.07 MJ, confinement time from 0.112 s to 0.152 s, volume averaged normalized beta from 1.65 to 1.82, and the HL89 H-factor from 1.45 to 1.76. These changes will subsequently be shown as consistent with interpreted transport parameters.

Figure 3 shows the reversal of the I-coil current in the upper I-coil located at 30° (from North) around the tokamak for DIII-D shot 147170 which has $I_p = 1.6$ MA, $B_T = 1.9$ T, $\kappa = 1.8$, $\delta = 0.64$, $\nu^* = 0.09$, and q95 ~ 3.4. Also shown in Fig. 3 is the measured line average density, the fluctuations of which are clearly correlated with the reversal of toroidal phase of the I-coil current. Phase change of RMP may play an integral role in tokamak operation just under the ELM suppression threshold if this density fluctuation can be controlled.

ELM suppressed time slices representing each toroidal phase of the I-coil current chosen for analysis were 3115–3185 ms for the 60° phase and 3300–3380 ms for the 0° phase, as indicated by the vertical lines in Fig. 3. Though the core plasma parameters are changing between RMP
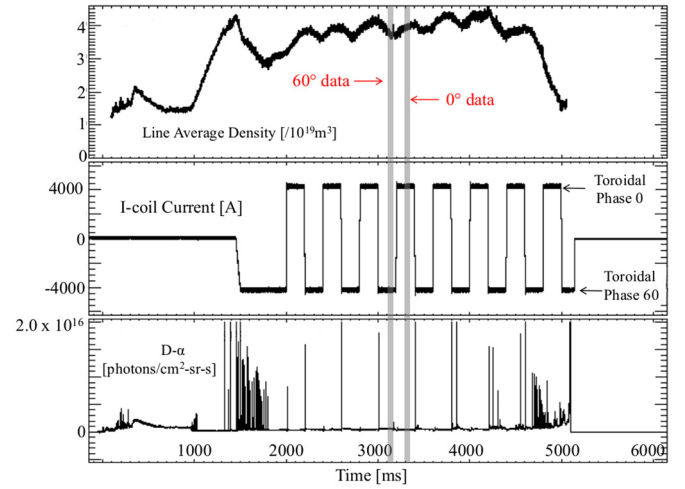

FIG. 3. Change in density associated with toroidal phase reversal in the I-coils and D-alpha signal showing ELM suppression during representative time slices.

phases, they remain relatively constant before and after the chosen representative 0° and 60° time slices. Time derivatives are then assumed to be insignificant for this analysis, making differences in pedestal parameters likely to be most influenced by the toroidal phase of the RMP currents and not by fluctuations in plasma core parameters.

Data for each time slice was obtained from the DIII-D database,[21] and spline fits of the data collected from the Charge Exchange Recombination (CER) system[22] were used to define the carbon ion impurity fraction, temperature, and toroidal and poloidal velocity profiles. Hyperbolic tangent fits were employed to fit the electron density, temperature, and pressure profiles measured by the Thomson scattering system.[23] As an example, the hyperbolic tangent fits of the electron density, and the experimental data are shown in Fig. 4 for both phases. Subsequently, the scale lengths and time derivatives were calculated for each profile.[24]

After relevant parameters were obtained from the DIII-D database and fitted, the GTEDGE pedestal code[25–27] was used to interpret various transport parameters for each time slice. This code performs calculations of three separate balance conditions for the edge plasma in order to determine the edge pedestal density radial profile. A particle and energy
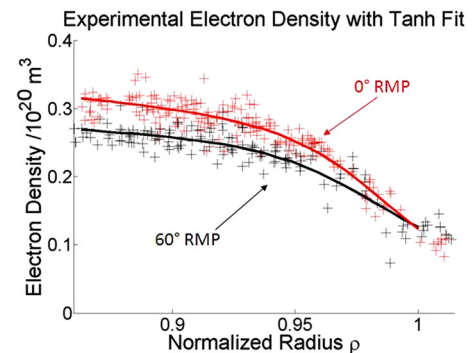

FIG. 4. Hyperbolic tangent fit for electron density [10^{20}/m^3] for 0° and 60° I-coil phases with measured densities represented by the symbol +. Representative error from the fit statistics from time averaging for this measurement is about 1×10^{18} m^{-3} in the edge pedestal region.

balance is applied to the core to determine the net ion flux across the separatrix. A two-dimensional neutral particle calculation using integral transport theory is used to determine the inward neutral particle flux across the separatrix. After calculating the inward and outward particle fluxes across the separatrix, the ion density at the separatrix is calculated using a "2-point" divertor model calculation. With these boundary conditions defined, the transport of neutrals refueling the plasma edge and the ion density profile are simultaneously calculated.[28] GTEDGE model parameters such as pedestal height, recycling neutrals source, particle confinement time, and synthesized density and temperature profile parameters are adjusted to predict the experimental plasma core line average density, energy confinement time, and central and edge pedestal temperatures. The normalized radius $\rho = r/a$ between $\rho = 0.86$ and $\rho = 1$ is divided into twenty-five discrete points, which are the locations where the quantities calculated in GTEDGE are defined. With this adjusted core plasma, the edge particle and energy fluxes can be calculated and used to interpret measured densities, temperatures, and rotation velocities, which can hence be interpreted in terms of the radial electric field, the pinch velocity, the particle diffusion coefficient, and the thermal diffusivities in the edge pedestal.

III. DIRECTLY MEASURED AND INFERRED EXPERIMENTAL PROFILES

Diagnostic systems at DIII-D allow for direct measurement of several key parameters used in the analysis of particle diffusion. These quantities include electron and carbon ion density, electron and carbon ion temperature, and carbon ion rotation velocities. The density and temperature profiles for electrons are measured using the Thomson Scattering system,[23] and velocity, temperature, and pressure gradient profiles of carbon impurities are measured with the CER spectroscopy system.[22]

The electron density shown in Fig. 4 displays a higher density and a larger density gradient for the 0° profile, which generates a more pronounced pedestal (located at around $\rho = 0.96$) as compared to the 60° profile. Because the density profile in the plasma edge is a key contributor to the diffusive and non-diffusive transport discussion, Fig. 4 will be a reference for comparison to many of the later profiles analyzed.

Ion and electron temperature profiles in Fig. 5 are similar for the 0° and 60° phases. The electron temperature profile has a sharper gradient, giving rise to a more pronounced pedestal, again around $\rho = 0.96$. The lack of ELMs in experimental measurements for these time slices indicates that both phases have suppressed ELMs by RMPs, meaning the product of this temperature profile and the density profile is small enough to be within the peeling-ballooning mode ELM stability limits. Stability calculations using the ELITE code[3,29] are needed to see where these profiles reside with respect to the linear peeling-ballooning stability boundary.

Experimental profiles are used with classical conservation law constraints in order to calculate additional experimental values as well as infer transport coefficients. Plasma
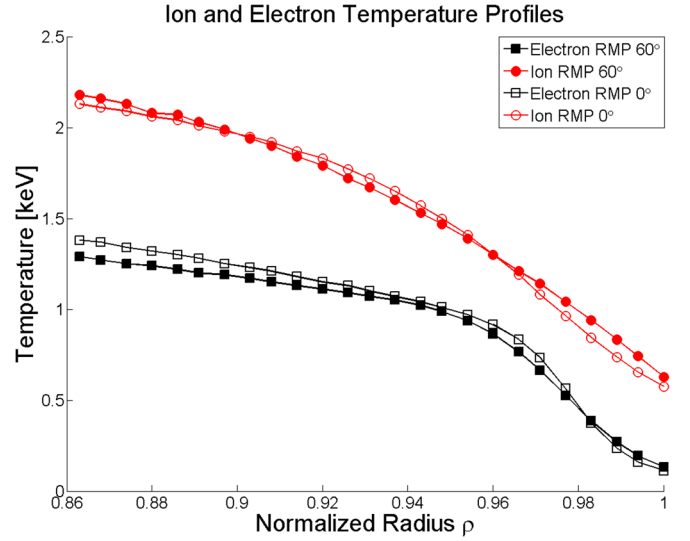

FIG. 5. Measured ion and electron temperature profiles as a function of normalized radius.

fluid theory based on the first four velocity moments of the Boltzmann transport equation is used to define constraints for interpretation of the transport underlying the measured density, temperature, and rotation profiles.[30] The constraints on plasma ion transport are (1) particle continuity, (2) momentum balance, (3) conservation of energy, and (4) heat conductivity.

Taking the 0th velocity moment of the Boltzmann equation and assuming time independence, the first constraint on transport is obtained: particle continuity or particle balance for the main ion species j[15]

$$\nabla \cdot \Gamma = \nabla \cdot n_j v_j = S_j, \tag{1}$$

where n_j is the density, v_j is the velocity, and S_j is the source, which is largely constructed from ionization of recycling neutrals, as well as external particle sources, such as Neutral Beam Injection (NBI). The source term is calculated in detail by Stacey,[27] using measured density, temperatures, and with neutral recycling sources adjusted to yield the measured line average density. Numerically integrating Eq. (1) inward from the separatrix leads to the experimental ion flux for particle species j, given in Fig. 6 for the two RMP phases.

The particle flux in the radial direction is larger for the 0° phase than for the 60° phase, consistent with the larger particle density for the 0° phase in Fig. 4 due to Eq. (1).

A radial momentum balance can be defined from the 1st velocity moment of the Boltzmann equation[15] and applied to the carbon ion. Carbon rotation velocity profiles are measured with the CER system in DIII-D,[22] therefore the radial electric field is the only unknown in the radial momentum balance in the below equation

$$E_r = \frac{1}{n_c e_c} \frac{\partial p_c}{\partial r} + V_{\Phi C} B_\theta - V_{\theta C} B_\Phi, \tag{2}$$

where E_r is the radial electric field, n_c is the carbon density, e_c is the charge of carbon, p_c is the carbon pressure, $V_{\varphi c}$ and $V_{\theta c}$ are respectively the toroidal and poloidal carbon rotation

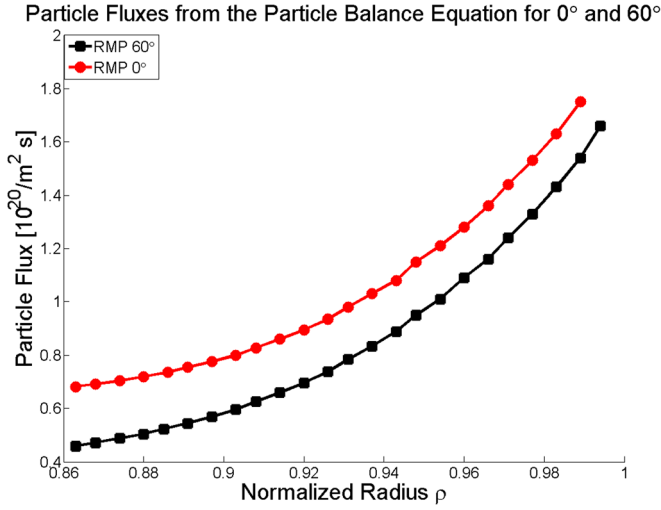Particle Fluxes from the Particle Balance Equation for 0° and 60°

FIG. 6. Ion fluxes calculated from the particle balance equation for 0° and 60°. Ion velocities and impurity fractions are measured using the CER system,[22] and electron densities are measured using the Thomson scattering system.[23]

velocities, and B_θ and B_φ are the respectively the poloidal and toroidal magnetic fields. The radial electric field is significantly different between the two phases of the I-coil, as shown in Fig. 7.

The radial electric field for the I-coil phase 60° remains negative for $\rho > 0.93$, while the 0° case becomes positive again just inside the separatrix at about $\rho = 0.98$, which can be attributed to the larger density gradient (and therefore pressure gradient) for the 0° phase seen in Fig. 4. The profile change of the electric field between RMP phases will be shown to affect the particle pinch velocity and thus have an important effect on transport, and hence on the density profiles. Deuterium poloidal velocity profiles are calculated from the deuterium radial momentum balance using the radial electric field profiles shown in Fig. 7.

One major observation is the shift in location of the "well" between phase profiles. This may be due in part to
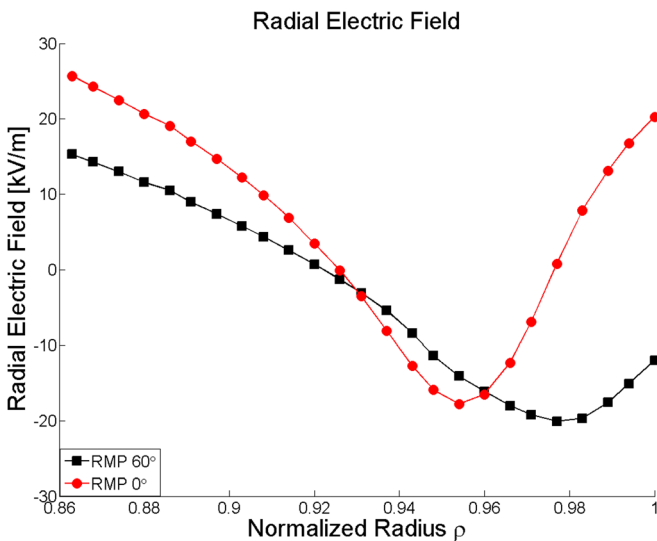
data processing from the original measured data, where the boundary condition of the electron temperature is assumed to be 50 eV at a normalized flux surface equal to one (the separatrix). However, this shift was not applied to the ion profiles, therefore not affecting the velocity profiles from which this electric field is calculated. This electron shift is a common practice for diagnostics in tokamaks, but remains an issue to be examined in future analysis, possibly causing errors in the alignment of profiles, such as the radial electric field.

In the DIII-D tokamak, the carbon toroidal and poloidal velocities are measured, and the deuterium velocities must be calculated. The deuterium and carbon toroidal velocities are frequently found to be comparable, allowing a first order perturbation analysis[31] to be used to obtain the toroidal velocity profile for deuterium,

$$V_{\Phi D} = V_{\Phi C} + \frac{(n_D e_D E_\Phi^A + e_D B_\theta \Gamma_D + M_{\Phi D}) - n_D \nu_{dD} V_{\Phi C}}{n_D m_D (\nu_{DC} + \nu_{dD})},$$
(3)

where n is density, e is charge, E^A is the induced toroidal electric field, Γ is the particle flux calculated from Eq. (1), M is the externally injected momentum, and the ν quantities are toroidal momentum transport frequencies, which are composite parameters dependent upon charge exchange, viscosity, inertia, and other anomolous processes.

Poloidal deuterium velocities are obtained by again rearranging Eq. (2), this time balancing the deuterium ion momentum[32]

$$V_{\theta D} = \frac{1}{B_\Phi} \left(B_\theta V_{\Phi D} + \frac{1}{n_D e_D} \frac{\partial p_D}{\partial r} - E_r \right).$$
(4)

Through measurement and momentum constraints, the poloidal and toroidal velocities for both carbon and deuterium have been determined, as well as the radial electric field. The radial deuterium particle flux has been determined through

Radial Electric Field

FIG. 7. Measured radial electric field [kv/m] as a function of normalized radius.
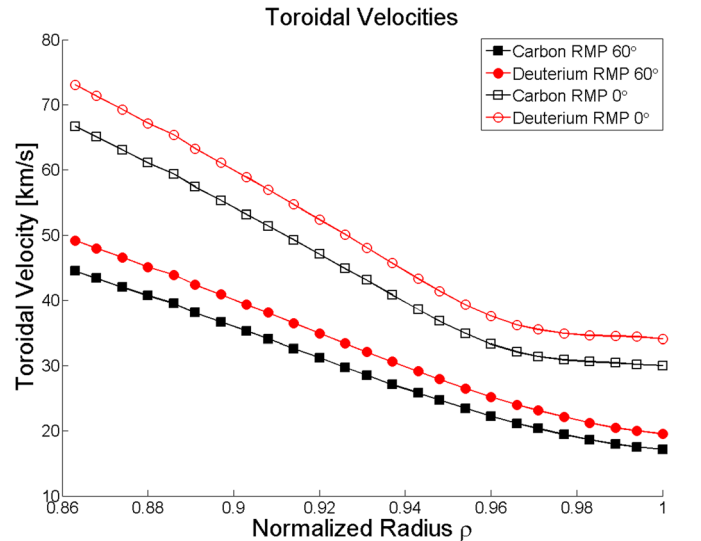
Toroidal Velocities

FIG. 8. Toroidal rotation velocities [km/s] for both measured carbon and calculated deuterium ions in the 0° and 60° phases.
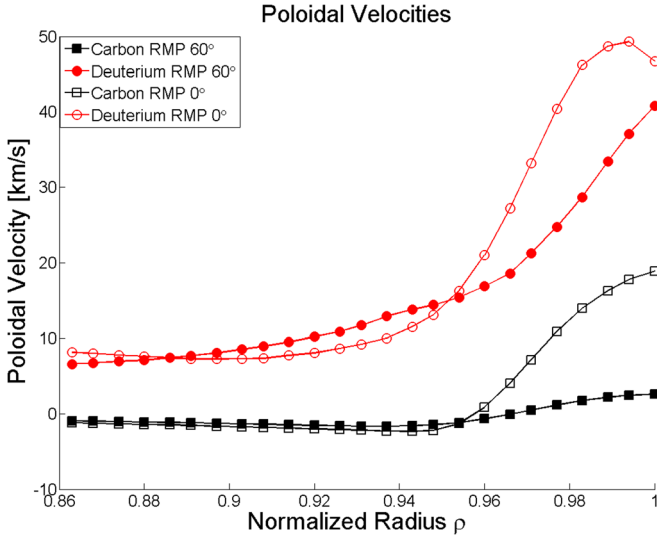
FIG. 9. Poloidal rotation velocities for measured carbon and calculated deuterium ions for 0° and 60°.

particle conservation. Toroidal velocities for both carbon and deuterium are shown in Fig. 8.

An increase in both toroidal rotation velocity and its gradient can be seen for the 0° relative to the 60° phase in both the carbon and deuterium velocity profiles. Carbon and deuterium velocity profiles for both phases are similar enough to validate the use of perturbation theory shown in Eq. (3).

Poloidal rotation velocities, shown in Fig. 9, are similar between phases for $\rho < 0.96$. However, for $\rho > 0.96$, the poloidal rotation velocity is significantly larger for the 0° phase for both carbon and deuterium.

IV. INFERRED PARTICLE TRANSPORT IN THE EDGE PEDESTAL

The toroidal momentum balance equation introduces momentum transport or "drag" frequencies, which are not directly measured quantities. Drag frequencies are denoted with a "d" subscript, along with the designated ion subscript, and represent the momentum loss due to viscosity, charge exchange, inertia, and other "anomolous" forces.[32] The interspecies collision frequency is denoted by the subscript "DC," and accounts for the toroidal momentum transfer between deuterium and carbon. By using first order perturbation analysis of the toroidal and radial momentum balance equations, expressions for these momentum transfer frequencies in terms of the measured carbon rotation velocities and other known quantities can be derived[32]

$$\nu_{dD} = \frac{(n_D e_D E_\Phi^A + e_D B_\theta \Gamma_{rD} + M_{\Phi D}) + (n_C e_C E_\Phi^A + e_C B_\theta \Gamma_{rC} + M_{\Phi C})}{(n_D m_D + n_C m_C) V_{\Phi C}^{\exp}}, \tag{5}$$

$$\nu_{dC} = \frac{(n_C e_C E_\Phi^A + e_C B_\theta \Gamma_{rC} + M_{\Phi C}) + m_D n_D \nu_{DC}(V_{\Phi D} - V_{\Phi C})_0}{n_C m_C V_{\Phi C}^{\exp}}, \tag{6}$$

where the difference in toroidal velocity between the deuterium and the carbon is defined in the perturbation analysis above in Eq. (3), and Γ is the radial particle flux calculated from Eq. (1).

The deuterium drag frequencies and collision frequencies describing toroidal momentum transfer are shown in Fig. 10, where it is shown that the momentum transport across flux surfaces by viscosity, charge exchange, etc., dominates collisional momentum transfer between ion species. This figure shows that deuterium drag is the dominant mechanism for toroidal momentum transfer and will subsequently be shown to determine radial diffusion.

Rearranging these momentum balance equations, a pinch diffusion expression for the radial particle flux, Γ, can be obtained[32]

$$\Gamma_D = n_D V_D = -\frac{n_D D_D}{p_D} \frac{\partial p_D}{\partial r} + n_D V_{rD}^{pinch}, \tag{7}$$

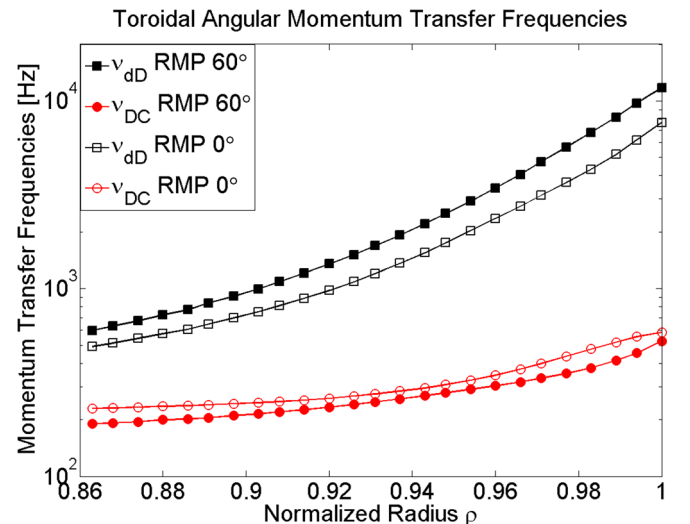where the diffusion coefficient, D, is defined as[32]

FIG. 10. Calculated toroidal angular momentum transfer frequency ν_{dD} and interspecies collision frequency, ν_{DC}.

$$D_D = \frac{m_D T_D \nu_{DC}}{(e_D B_\theta)^2}\left(1 + \frac{\nu_{dD}}{\nu_{DC}} - \frac{e_D}{e_C}\right), \tag{8}$$

and the pinch velocity is[32]

$$V_{rD}^{pinch} = \frac{\left[-M_{\Phi D} - n_D e_D E_\Phi^A + n_D m_D (\nu_{DC} + \nu_{dD})\left(\frac{B_\Phi V_{\theta D}}{B_\theta} + \frac{E_r}{B_\theta}\right) - n_D m_D \nu_{DC} V_{\Phi C}\right]}{n_D e_D B_\theta}. \tag{9}$$

It is clear from Eq. (7) that the ion flux consists of a "standard" outward diffusive component from the deuterium ion pressure gradient (and therefore density and temperature gradients), as well as an inward non-diffusive, "pinch" term defined by Eq. (9). The diffusive term is normally outward, and non-diffusive pinch term can be either inward or outward. This derived pinch diffusion relation in Eq. (7) has the same form as the standard ad-hoc pinch diffusion relation, except for having a thermal diffusion term in addition to the density diffusion term. From the momentum balance, the pinch term is associated with $\mathbf{V} \times \mathbf{B}$, E_r, and other terms in Eq. (9) that can be determined from experiment.

Returning to Fig. 10, it is seen that deuterium drag frequencies for 60° are larger than for the 0° case, resulting in larger outward diffusion coefficients for the 60° case than for the 0° case, as shown in Fig. 11.

The pinch velocity profiles, which are constructed using measured and calculated data to evaluate Eq. (8), become strongly negative (inward) in the plasma edge as shown in Fig. 12. Negative pinch velocities indicate an inward electromagnetic force and inward non-diffusive particle flux, which is significantly stronger for the 60° phase than for the 0° phase.

Momentum transfer frequencies, radial electric field, rotation velocities, as well as other factors all influence the pinch velocity profiles shown in Fig. 12. The decomposition of the dependence of the pinch velocity on each term in Eq. (9) can be seen for the 0° and 60° phases in Figs. 13 and 14, respectively.
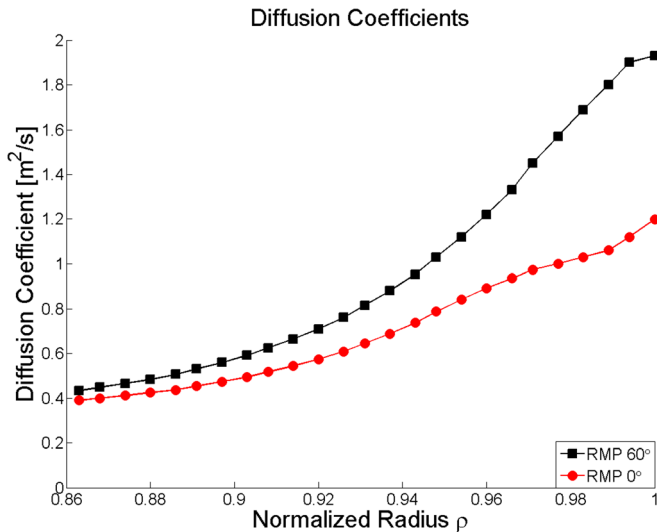
Poloidal velocity plays a key role in defining the pinch velocity for each phase, with a large negative Vpinch contribution for $\rho > 0.96$. This is the same region where the calculated poloidal velocity profile notably increased for deuterium ions in Fig. 9. The radial electric field component of the pinch velocity is also an important term, enhancing the negative electric field component for the 60° phase and partially cancelling it for the for the 0° phase. These radial electric field
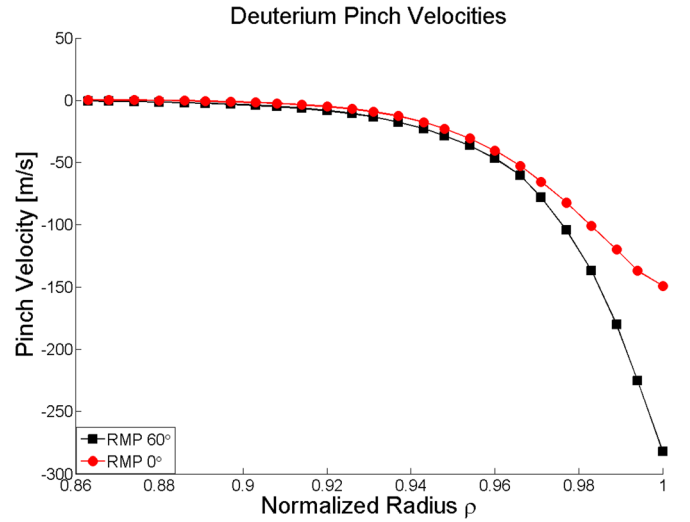

FIG. 12. Calculated inward pinch velocity for 60° and 0°.

FIG. 11. Calculated radially outward diffusion coefficients as a function of normalized radius.

FIG. 13. Decomposition of components of calculated Vpinch for 0° with terms depending on NBI and toroidal electric field, radial electric field, poloidal velocity, and toroidal velocity. The 'Beam and Ephi' and 'Vphi' terms contribute nearly zero, and the 'Erad' is the only positive contribution.
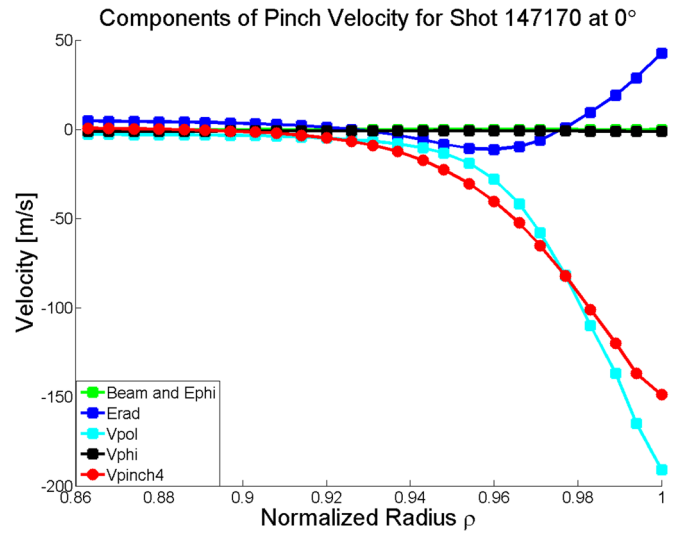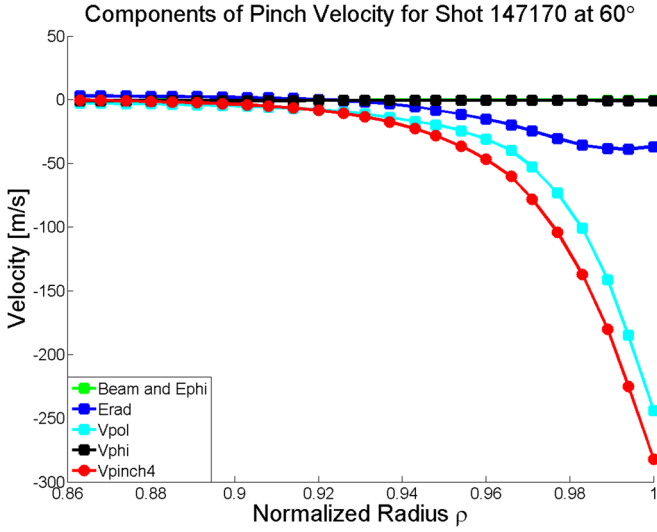
FIG. 14. Decomposition of components of calculated Vpinch for 60° into terms depending on NBI and toroidal electric field, radial electric field, poloidal velocity, and toroidal velocity. The 'Beam and Ephi' and 'Vphi' terms contribute nearly zero, and the 'Erad' term is the slightly negative contribution around −50 m/s.

contributions reflect the sign of the field profiles shown in Fig. 7.

The two major components of poloidal velocity and radial electric field are the only two terms that contain the toroidal drag frequency. Since the toroidal drag frequency dominates the collision frequency, the poloidal velocity, and radial electric field terms are more important in the expression for pinch velocity. Since the 60° drag frequencies are larger than those of 0°, it is expected that the pinch velocity will be larger, which is confirmed in Fig. 12.

Particle fluxes can be analyzed by looking at the diffusive components compared to the non-diffusive pinch components; however, it is first necessary to correct for ion orbit loss. Ion orbit loss takes place when some thermalized plasma ions and energetic neutral beam ions (and fusion alpha particles) execute orbits that cross the last closed flux surface. These ions are assumed to be lost to the plasma and must be taken into account when interpretting measured data in terms of diffusive and non-diffusive transport processes taking place in the plasma.[33] The decomposition of particle fluxes in such a manner is shown in Fig. 15. Note that the profiles in Fig. 15(b) are the same as the flux profiles calculated in Fig. 6 except with the ion orbit loss correction.

The larger diffusion coefficients for the 60° case than for the 0° case shown in Fig. 11, together with the rather similar density profiles shown in Fig. 4, imply a larger outward diffusive flux for 60° than for 0°, which is consistent with the smaller density profile for the 60° phase. However, the inward non-diffusive pinch flux shown in Fig. 12 is also larger for the 60° phase, so that both the outward diffusive particle flux and the inward non-diffusive pinch transport are larger for the 60° phase, with values on the order of 10×10^{20} particles/m²s in the transport barrier region. The net outward diffusive plus non-diffusive flux is smaller for the 60° phase than for the 0° phase and is on the order of 1×10^{20} particles/m²s, which means that this cancellation could be sensitive to
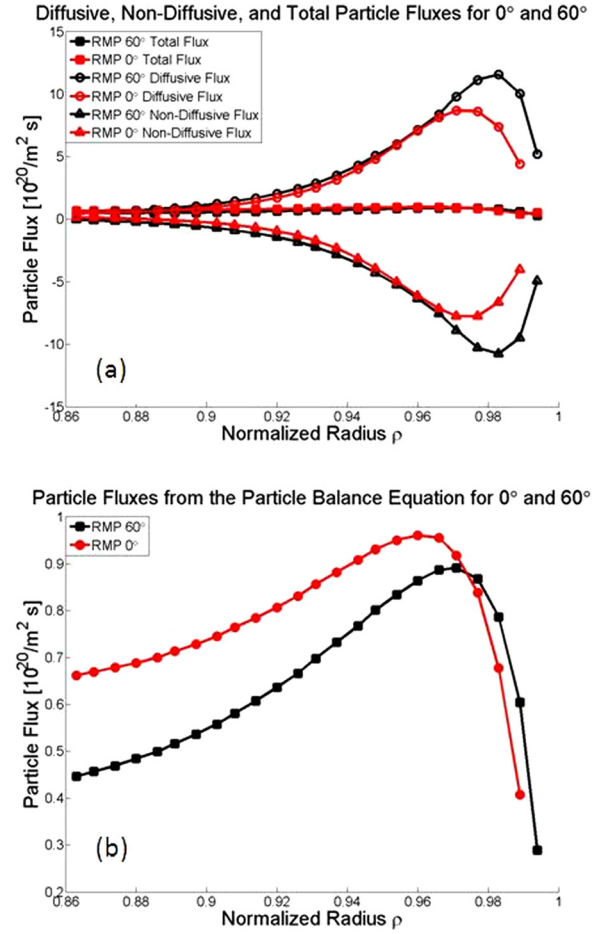

FIG. 15. (a) Calculated diffusive and non-diffusive pinch particle flux components of total flux with ion orbit loss correction. The 60° phase has a larger magnitude for both diffusive and non-diffusive flux than the 0° phase. (b) Net flux with the ion orbit loss correction.

uncertainties in edge measurements. The larger cancellation of particle flux for 60° is associated with a lower edge pedestal density for 60° as compared to 0°. Understanding the underlying mechanisms which determine the pinch velocity and radial diffusion coefficient, such as the dependence on the toroidal angular momentum transfer frequencies and ion orbit loss, is important for understanding how the RMP controls the edge density and thereby suppresses ELMs.

As a consistency check, a comparison is made between the radial ion particle fluxes calculated using the experimental data to solve the continuity equation of Eq. (1) with those obtained by using the experimental and calculated data to evaluate the pinch diffusion relation of Eq. (7). Note that the two radial fluxes without the ion orbit loss correction are the total radial fluxes calculated from integrating the continuity equation or by evaluating the pinch diffusion relation with experimental measurements. A fraction of this total flux is due to outstreaming by ion orbit loss, and should not be included in the total transport flux. The remaining flux that is not caused by ion orbit loss is shown in the corrected curves, and is associated solely with the outward transport of particles. These fluxes, with and without corrections for ion orbit loss,[33] are shown in Fig. 16 for both phases.

It is clear that there is agreement between the two calculations of flux, and for each phase the average discrepancy is
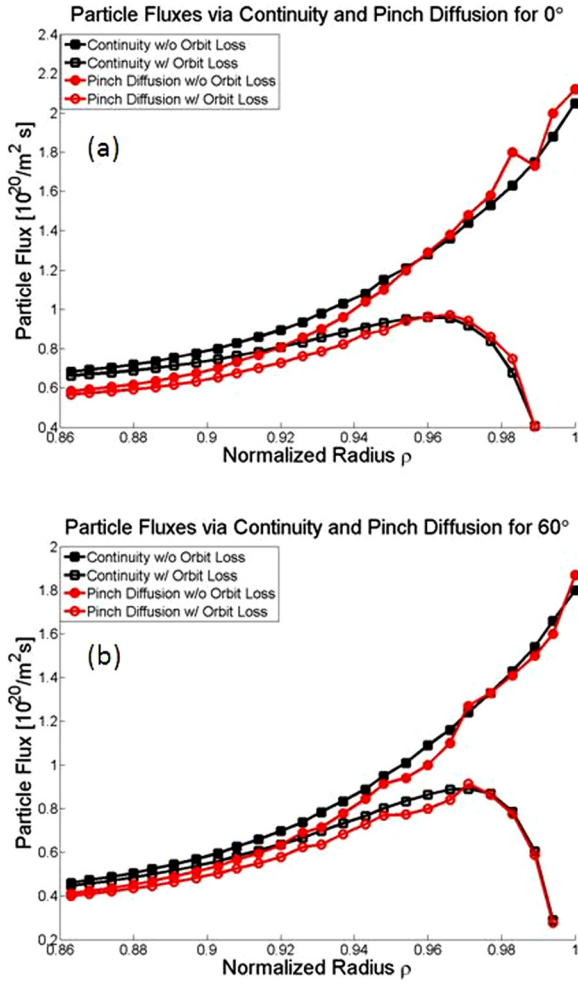
FIG. 16. Comparison of particle fluxes with and without orbit loss calculated via the continuity equation and the pinch diffusion relation for (a) 0° and (b) 60°.

within 8.5%, with the largest discrepancy being just under 15% at the beginning of the profiles most likely due to boudary condition constraints used in the calculation.

V. THERMAL TRANSPORT

Previous analysis has shown that pressure gradients for DIII-D RMP shots with n = 3 I-coil perturbations sometimes have been reduced due to density decrease without an effective change in energy transport,[4] while others have displayed a temperature modulation affecting pressure gradients.[6] Thermal transport is an important part of plasma edge analysis and the formation of transport barriers, and therefore it is necessary to calculate the effect of the difference in toroidal phase on the inferred thermal diffusivities. Plasma edge analysis is further constrained by conserving energy. The 2nd velocity moment of the Boltzmann equation is the conservation of energy for both the ions (D,C) and electrons (e)[32]

$$\frac{\partial Q_D}{\partial r} = -\frac{\partial}{\partial t}\left(\frac{3}{2}n_D T_D\right) + q_{nbD} - q_{De}$$
$$- n_e n_0^C \langle \sigma v \rangle_{cx} \frac{3}{2}(T_D - T_0^C), \quad (10)$$

$$\frac{\partial Q_e}{\partial r} = -\frac{\partial}{\partial t}\left(\frac{3}{2}n_e T_e\right) + q_{nbe} + q_{De} - n_e n_C L_C(T_e), \quad (11)$$

where the total heat flux is Q = q + (3/2) Γ T and q is the conductive heat flux. The souce of ion energy is NBI or other external heating (about 8 MW for this discharge), and the sinks include collisions with electrons and charge exchange. The energy sources for electrons are external heating and the energy transferred from ions, while energy may be lost due to radiative cooling.[32]

The 3rd velocity moment of the Boltzmann equation constrains heat conduction, however for simplicity, the familiar heat conduction relation shown in below equation for both the deuterium ion and electrons is used in lieu of the complex third velocity moment equation

$$q_{D,e} = -n_{D,e}\chi_{D,e}\frac{\partial T_{D,e}}{\partial r}. \quad (12)$$

Using Eqs (10)–(12) to solve for the ion and electron heat fluxes and the calculated particle fluxes from the 0th moment constraint, the experimental heat diffusivities for both ions and electrons can be inferred from the measured temperature profiles

$$\chi_{D,e} = -\frac{Q_{D,e}^{\exp}(1 - E_{orbD}) - \frac{3}{2}\Gamma_{D,e}^{\exp}(1 - F_{orbD})T_{D,e}^{\exp}}{n_{D,e}^{\exp}\left(\frac{\partial T_{D,e}^{\exp}}{\partial r}\right)}, \quad (13)$$

where F_{orbD} is the cumulative fraction of the radial ion flux lost by ion orbit loss in the edge, and E_{orbD} is a similarly defined ion orbit energy loss fraction. Neither of these ion orbit loss fractions appear in the electron version of Eq. (13).

Inferred electron thermal diffusivities are shown in Fig. 17. The strong dip in the pedestal region of the experimental diffusivity profiles implies the presence of an energy transport barrier around $\rho = 0.96$. This thermal transport barrier aligns with the pinch velocity inward electromagnetic force barrier discussed previously in Fig. 12. The electron thermal diffusivity is much larger for $\rho < 0.92$ in the 60° case, but the two phases have similar thermal diffusivities in the outer pedestal region.
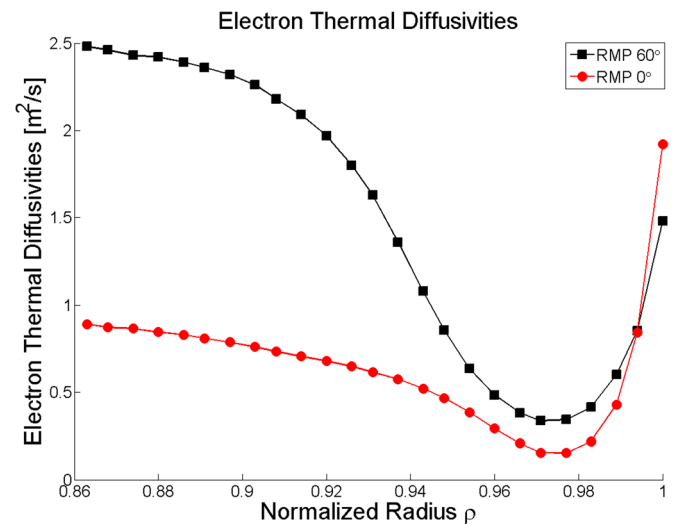

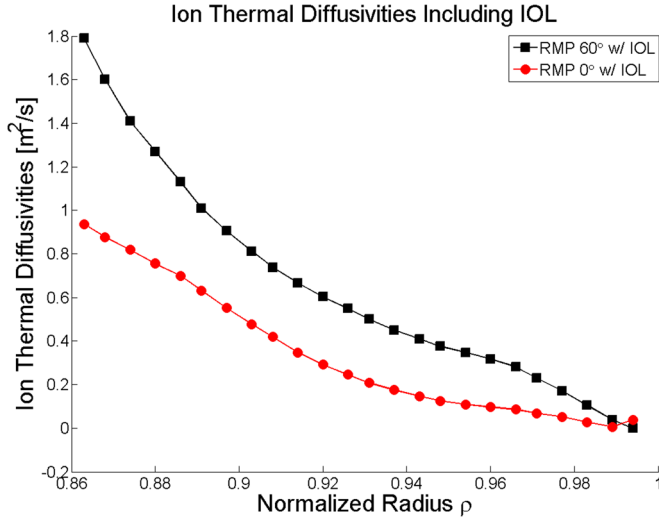FIG. 17. Inferred electron thermal diffusivities for 60° and 0°.

FIG. 18. Inferred ion thermal diffusivities for $0°$ and $60°$ phases with the inclusion of the ion orbit loss correction.

Ion thermal diffusivities, shown in Fig. 18, also show a trend for higher values for the $60°$ situation, however not with as great a difference as the electron diffusivities. (The total ion particle and heat fluxes used in Eq. (13) are reduced by the ion orbit loss fractions.)

The constant decreasing thermal diffusivity trend does not suggest as much of an energy transport barrier for ions as did the electron thermal diffusivity profiles, especially for the $60°$ profile. The inferred thermal diffusivities shown in Figs. 17 and 18, together with the similar temperature profiles in Fig. 5, imply larger diffusive heat transport for the $60°$ phase.

VI. INTRINSIC ROTATION

When analyzing ion orbit momentum loss, it has been recognized[34,35] that momentum loss in the edge occurs in a preferential direction, usually counter-current for anti-parallel toroidal current and magnetic field, leaving more particles in the plasma with co-current rotation velocities. A counter-current sink in momentum appears as an increase in intrinsic co-current rotation in the plasma edge. An expression for the increase in toroidal rotation velocity can be shown to be[34]

$$\Delta V_{\Phi} = \frac{2}{\sqrt{\pi}} M_{orb}(\rho) V_{th}(\rho), \qquad (14)$$

where M_{orb} is the cumulative momentum loss fraction,[33] and V_{th} is the ion thermal velocity. Intrinsic rotation, shown in Fig. 19(a), is induced more for the $0°$ RMP phase because the momentum loss fraction is larger, while the ion temperatures are similar for the two phases.

The maximum increase in deterium toroidal velocity due to ion orbit loss for $0°$ is roughly 5×10^4 m/s at $\rho = 0.97$, implying that RMPs may cause intrinsic rotation in tokamaks. The calculated changes in deuterium intrinsic toroidal velocity for the $0°$ case is about the same. This is suggestive that ion orbit loss could be causal for the observed differences in toroidal velocity between the two phases. However, there may be other mechanisms, such as torque
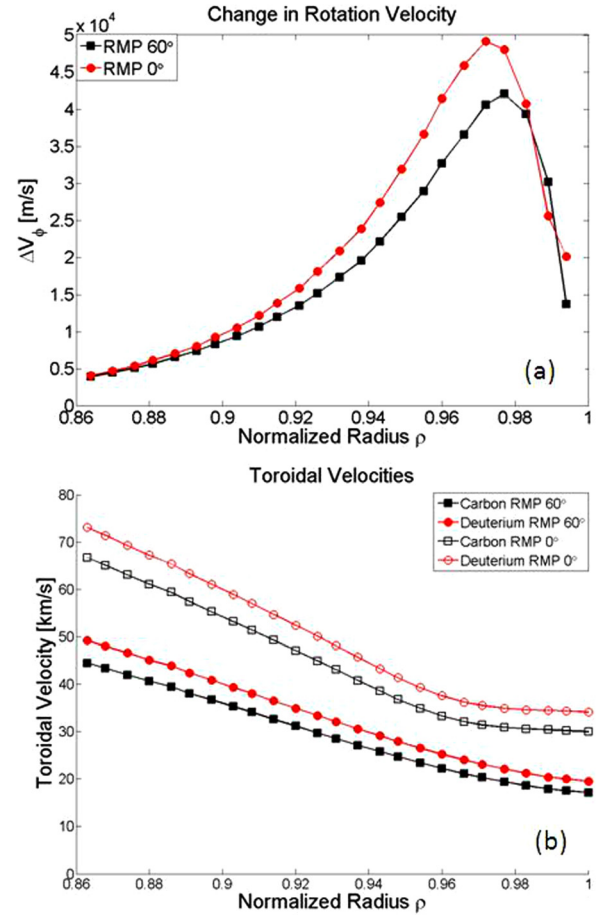

FIG. 19. (a) Calculated change in deuterium toroidal rotation velocity due to ion orbit loss. (b) Measured carbon and calculated deuterium toroidal velocities.

from the radial magnetic field perturbation, that are more dominant.

VII. CONCLUSIONS

Repeated reversals of resonant magnetic perturbations of the I-coil between $0°$ and $60°$ toroidal phases in DIII-D shot 147170 generate different edge pedestal profiles. Measured density, temperature, and rotation profile variations can be interpreted as differences in diffusive and non-diffusive transport, resulting in a theoretical basis for a better understanding of RMP toroidal phase effects on pedestal transport.

Large outward diffusive particle fluxes and comparably large inward electromagnetic particle pinches are found for both RMP toroidal phases. The opposing fluxes compensate each other and produce a net outward particle flux smaller than its diffusive and non-diffusive components by an order of magnitude. The net outward particle flux is found to be larger for the $0°$ than for the $60°$ RMP phase, consistent with the larger density for $0°$. The $60°$ phase has both larger diffusive and non-diffusive flux components than in the $0°$ phase. The particle fluxes found from evaluating the pinch-diffusion relation using experimental data agree with the fluxes obtained by solving the continuity equation for both toroidal RMP phases, confirming the internal consistency of this analysis.

Electron and ion thermal diffusivities inferred from the density and temperature profiles are similar for the two toroidal phases in the steep-gradient pedestal region, but differ in the flattop region further inward, where the $60°$ phase is larger than the $0°$ phase for both species. The electron thermal diffusivity profiles exhibited a "transport barrier" well just inside the separatrix.

Toroidal momentum transport frequencies, or "drag" frequencies, are larger than interspecies collision frequencies and had a major effect on both the diffusive and non-diffusive transport. The $60°$ phase had larger inferred "drag" frequencies, which appeared to be the driving factor for the increased flux components for this phase. Since the toroidal magnetic field asymmetries were larger for the $0°$ phase than for the $60°$ phase, the magnetic asymmetry magnitude would not seem to be the cause for different transport between the two phases.

By interpreting the density and rotation velocity profiles, an argument can be made that the increased density for the $0°$ toroidal phase relative to the $60°$ phase may be ultimately driven by the larger intrinsic rotation velocity attributable to ion orbit loss. The larger toroidal velocity for $0°$ leads to an inference of smaller momentum transport "drag" frequencies, which results in smaller interpreted particle diffusion coefficients and pinch velocities for the $0°$ phase. The smaller diffusion coefficients for $0°$ lead to fewer particles leaving the plasma via diffusive processes for $0°$ than $60°$. Other plausible explanations, which have not been examined in this work, such as the torque from radial currents and the non-axisymmetry of the "background" or "error" radial magnetic field, may also play a role in driving intrinsic rotation.

For this analysis, increased transport was observed when the RMP toroidal phase destructively interfered with the "background" magnetic field, and an increase in confinement was seen for the phase with constructive interference. Future work includes applying the present analysis to a similar RMP shot in DIII-D with a nulled out interference, or $n = 0$, in the RMP fields between toroidal phases or an opposite case where the $60°$ RMP phase exhibits constructive interference with the "background" field to determine if similar trends occur.

[1]F. Wagner, G. Becker, K. Behringer, D. Campbell, A. Eberhagen, W. Engelhardt, G. Fussmann, O. Gehre, J. Gernhardt, G. v. Gierke, G. Haas, M. Huang, F. Karger, M. Keilhacker, Q. Kluber, M. Kornherr, K. Lackner, G. Lisitano, G. G. Lister, H. M. Mayer, D. Meisel, E. R. MIiller, H. Murmann, H. Niedermeyer, W. Poschenrieder, H. Rapp, H. Bohr, F. Schneider, G. Siller, E. Speth, A. Stabler, K. H. Steuer, G. Venus, O. Vollmer, and Z. Yu, Phys. Rev. Lett. **49**, 1408 (1982).

[2]H. Zohm, Plasma Phys. Controlled Fusion **38**, 105 (1996).

[3]T. E. Evans, "ELM mitigation techniques," J. Nucl. Mater. (in press).

[4]T. E. Evans, R. A. Moyer, K. H. Burrell, M. E. Fenstermacher, I. Joseph, A. W. Leonard, T. H. Osborne, G. D. Porter, M. J. Schaffer, P. B. Snyder, P. R. Thomas, J. G. Watkins, and W. P. West, Nature Physics **2**, 419 (2006).

[5]W. M. Stacey and T. E. Evans, Nucl. Fusion **51**, 013007 (2011).

[6]O. Schmitz, T. E. Evans, M. E. Fenstermacher, E. A. Unterberg, M. E. Austin, B. D. Bray, N. H. Brooks, H. Frerichs, M. Groth, M. W. Jakubowski, C. J. Lasnier, M. Lehnen, A. W. Leonard, S. Mordijck, R. A. Moyer, T. H. Osborne, D. Reiter, U. Samm, M. J. Schaffer, B. Unterberg, W. P. West, and DIII-D and TEXTOR Research Teams, Phys. Rev. Lett. **103**, 165005 (2009).

[7]E. Nardon, M. Becoulet, G. Huysmans, O. Czarny, P. R. Thomas, M. Lipa, R. A. Moyer, T. E. Evans, G. Federici, Y. Gribov, A. Polevoi, G. Saibene, A. Portone, and A. Loarte, Nucl. Mater. **363–365**, 1071 (2007).

[8]T. E. Evans, R. A. Moyer, J. G.Watkins, T. H. Osborne, P. R. Thomas, M. Becoulet, J. A. Boedo, E. J. Doyle, M. E. Fenstermacher, K. H. Finken, R. J. Groebner, M. Groth, J. H. Harris, G. L. Jackson, R. J. La Haye, C. J. Lasnier, S. Masuzaki, N. Ohyabu, D. G. Pretty, H. Reimerdes, T. L. Rhodes, D. L. Rudakov, M. J. Schaffer, M. R. Wade, G. Wang, W. P. West, and L. Zeng, Nucl. Fusion **45**, 595 (2005).

[9]P. Gohil, T. E. Evans, J. R. Ferron, R. A. Moyer, C. C. Petty, K. H. Burrell, T. A. Casper, A. M. Garofalo, A. W. Hyatt, R. J. Jayakumar, C. Kessel, J. Y. Kim, R. J. La Haye, J. Lohr, T. C. Luce, M. A. Makowski, D. Mazon, J. Menard, M. Murakami, P. A. Politzer, R. Prater, and M. R. Wade, Plasma Phys. Controlled Fusion **48**, A45 (2006).

[10]B. Hudson, T. E. Evans, C. Petty, and P. Snyder, Nucl. Fusion **50**, 064005 (2010).

[11]T. E. Evans, M. E. Fenstermacher, R. A. Moyer, T. H. Osborne, J. G. Watkins, P. Gohil, I. Joseph, M. J. Schaffer, L. R. Baylor, M. Bécoulet, J. A. Boedo, K. H. Burrell, J. S. deGrassie, K. H. Finken, T. Jernigan, M. W. Jakubowski, C. J. Lasnier, M. Lehnen, A. W. Leonard, J. Lonnroth, E. Nardon, V. Parail, O. Schmitz, B. Unterberg, and W. P. West, Nucl. Fusion **48**, 024002 (2008).

[12]T. E. Evans, R. A. Moyer, J. G. Watkins, P. R. Thomas, T. H. Osborne, J. A. Boedo, M. E. Fenstermacher, K. H. Finken, R. J. Groebner, M. Groth, J. Harris, G. L. Jackson, R. J. La Haye, C. J. Lasnier, M. J. Schaffer, G. Wang, and L. Zeng, Nucl. Mater. **337–339**, 691 (2005).

[13]J. D. Callen, A. J. Cole, and C. C. Hegna, Nucl. Fusion **49**, 085021 (2009).

[14]L. Frassinetti, S. Menmuir, K. E. J. Olofsson, P. R. Brunsell, and J. R. Drake, Nucl. Fusion **52**, 103014 (2012).

[15]W. M. Stacey, Contrib. Plasma Phys. **48**, 94 (2008).

[16]J. D. Callen, A. J. Cole, C. C. Hegna, S. Mordijck, and R. A. Moyer, Nucl. Fusion **52**, 114005 (2012).

[17]R. A. Moyer, T. E. Evans, T. H. Osborne, P. R. Thomas, M. Becoulet, J. Harris, K.-H. Finken, J. A. Boedo, E. J. Doyle, M. E. Fenstermacher, P. Gohil, R. J. Groebner, M. Groth, G. L. Jackson, R. J. La Haye, C. J. Lasnier, A. W. Leonard, G. R. McKee, H. Reimerdes, T. L. Rhodes, D. L. Rudakov, M. J. Schaffer, P. B. Snyder, M. R. Wade, G. Wang, J. G. Watkins, W. P. West, and L. Zeng, Phys. Plasmas **12**, 056119 (2005).

[18]T. E. Evans, R. A. Moyer, and P. Monat, Phys. Plasmas **9**, 4957 (2002).

[19]J. L. Luxon, M. J. Schaffer, G. L. Jackson, J. A. Leuer, A. Nagy, J. T. Scoville, and E. J. Strait, Nucl. Fusion **43**, 1813 (2003).

[20]T. E. Evans, "Changes in fluctuations and transport due to toroidal phase variations of non-axisymmetric magnetic perturbations in DIII-D," paper presented at the US Transport Taskforce Workshop, TTF, Annaplois, MD 10-13 April 2012.

[21]G. Bramson, D. P. Schissel, J. C. DeBoo, and H. St. John, Rev. Sci. Instumr. **61**, 3562 (1990).

[22]W. M. Solomon, K. H. Burrell, P. Gohil, R. J. Groebner, and L. R. Baylor, Rev. Sci. Instrum. **75**, 3481 (2004).

[23]T. N. Carlstrom, G. L. Campbell, J. C. DeBoo, R. Evanko, J. Evans, C. M. Greenfield, J. Haskovec, C. L. Hsieh, E. McKee, R. T. Snider, R. Stockdale, P. K. Trost, and M. P. Thomas, Rev. Sci. Instrum. **63**, 4901 (1992).

[24]T. H. Osborne, P. B. Snyder, K. H. Burrell, T. E. Evans, M. E. Fenstermacher, A. W. Leonard, R. A. Moyer, M. J. Schaffer, and W. P. West, J. Phys. Conf. Ser. **123**, 012014 (2008).

[25]W. M. Stacey, Phys. Plasmas **5**, 1015 (1998).

[26]W. M. Stacey, Phys. Plasmas **8**, 3673 (2001).

[27]W. M. Stacey, Nucl. Fusion **40**, 965 (2000).

[28]W. M. Stacey, Phys. Plasmas **11**, 4295 (2004).

[29]P. Helander, R. J. Akers, and L.-G. Eriksson, Phys. Plasmas **12**, 112503 (2005).

[30]W. M. Stacey, Fusion Sci. Technol. **63**, 34 (2013).

[31]W. M. Stacey and R. J. Groebner, Phys. Plasmas **15**, 012503 (2008).

[32]W. M. Stacey, R. J. Groebner, and T. E. Evans, Nucl. Fusion **52**, 114020 (2012).

[33]W. M. Stacey, Phys. Plasmas **18**, 102504 (2011).

[34]W. M. Stacey, J. A. Boedo, T. E. Evans, B. A. Grierson, and R. J. Groebner, Phys. Plasmas **19**, 112503 (2012).

[35]J. S. deGrassie, S. H. Muller, and J. A. Boedo, Nucl. Fusion **52**, 013010 (2012).